Probing the limits of the rigid-intensity-shift model in differential-phase-contrast scanning transmission electron microscopy

L. Clark,[1,*] H. G. Brown,[1] D. M. Paganin,[1] M. J. Morgan,[1] T. Matsumoto,[2] N. Shibata,[2] T. C. Petersen,[1] and S. D. Findlay[1]
[1]*School of Physics and Astronomy, Monash University, Victoria 3800, Australia*
[2]*Institute of Engineering Innovation, University of Toyko, Toyko 113-8656, Japan*

(Received 19 January 2018; published 18 April 2018)

The rigid-intensity-shift model of differential-phase-contrast imaging assumes that the phase gradient imposed on the transmitted probe by the sample causes the diffraction pattern intensity to shift rigidly by an amount proportional to that phase gradient. This behavior is seldom realized exactly in practice. Through a combination of experimental results, analytical modeling and numerical calculations, using as case studies electron microscope imaging of the built-in electric field in a p-n junction and nanoscale domains in a magnetic alloy, we explore the breakdown of rigid-intensity-shift behavior and how this depends on the magnitude of the phase gradient and the relative scale of features in the phase profile and the probe size. We present guidelines as to when the rigid-intensity-shift model can be applied for quantitative phase reconstruction using segmented detectors, and propose probe-shaping strategies to further improve the accuracy.

DOI: 10.1103/PhysRevA.97.043843

I. INTRODUCTION

In a transmission-based imaging system (using, for example, visible light, x rays, or electrons), the sample is interrogated by some radiation, which then propagates to a detector, generating a signal. The sample may absorb some of the probe quanta, or scatter them beyond the angular range of the detector, which may easily be measured as a reduction in the transmitted intensity. However, many samples of interest do not strongly change the detected intensity, instead only passing information to the beam in terms of phase shifts in the transmitted probe quanta (such as grating imperfections in visible-light microscopy, soft tissues such as lungs in x-ray imaging, or magnetic fields in transmission electron microscopy [1–3]). Such materials are referred to as phase objects, and their effect on the radiation field may be described with a transmission function [$T(x,y)$, with x and y denoting the coordinates in the plane of the specimen] that takes the form of a multiplicative phase factor:

$$\begin{aligned}\Psi_{\text{exit}}(x,y) &= \Psi_{\text{entrance}}(x,y)T(x,y)\\ &= \Psi_{\text{entrance}}(x,y)\exp[i\phi(x,y)],\end{aligned} \quad (1)$$

where $\Psi_{\text{entrance}}(x,y)$ is the wave function at the entrance surface of the specimen, $\Psi_{\text{exit}}(x,y)$ is the wave function as it leaves the specimen from the opposite face and $\phi(x,y)$ describes the sample-induced phase shift (wherein we have also assumed the sample to be thin, by which we mean that lateral spreading of the probe within the sample is negligible). As Eq. (1) makes clear, the imparted phase is lost if the exit wave function is imaged in focus. A range of techniques have been developed for a wide variety of probe quanta (visible light, x rays, electrons, neutrons) to convert this imparted phase to measurable intensity changes such as defocused imaging [4–6], holography [7–9], and differential phase contrast [10–15].

Differential-phase-contrast (DPC) imaging can be performed in a broad-beam single-shot mode [10–12] with tilted illumination, or in a focused-probe raster-scanned setup [13–15] with noncircularly symmetric detectors. This latter form has seen particular development recently in scanning transmission electron microscopy (STEM) as it is sensitive to atomic electric fields, nanometer-scale ferroelectric fields, and magnetic domains [16–18]. Using case studies drawn from nanoscale electromagnetic field mapping of materials in STEM, this manuscript explores the fundamental optical physics limitations on quantitative DPC imaging via segmented detectors that arise from the relative sizes of the probe and the features in the phase profile of the sample.

While the models chosen here exemplify systems appropriate to STEM, the approach we develop is applicable for coherent scanning-probe imaging using any of the aforementioned imaging quanta. This broad applicability regarding scanning-probe imaging using a coherent probe is enabled by the mathematical identity of the time-independent Helmholtz equation for unpolarized monochromatic scalar electromagnetic fields (such as visible light, extreme ultraviolet radiation, and hard x rays) in the presence of a scalar refractive index distribution, the time-independent Schrödinger equation for unpolarized electrons in the presence of a variable scalar potential, and the time-independent Klein-Gordon equation for unpolarized massive particles (such as neutrons) in the presence of a scalar medium.

In the scanning-transmission geometry we concentrate on herein, a probe is formed in the far field of a circular aperture, and focused upon a thin sample. If the detector is located in the diffraction plane of the sample, the intensity profile at the detector is

$$\begin{aligned}I(k_x,k_y) &= |\mathcal{F}[\Psi_{\text{exit}}(x,y)]|^2\\ &= |\Psi_{\text{entrance}}(k_x,k_y)\otimes\mathcal{F}\{\exp[i\phi(x,y)]\}|^2,\end{aligned} \quad (2)$$

*Corresponding author: laura.clark@monash.edu

 ©2018 American Physical Society

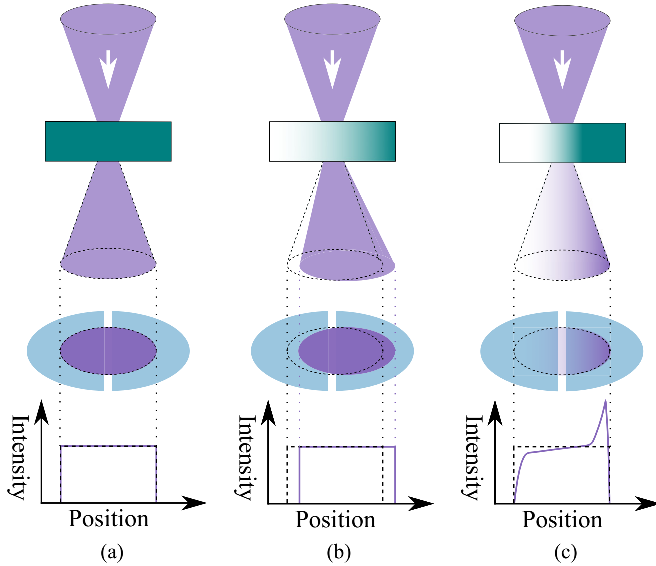

FIG. 1. DPC-STEM imaging. A probe is focused onto a thin phase object and scattered onto the detector below. (a) When $\nabla\phi = \vec{0}$, the diffraction pattern of the probe is unshifted. (b) When $\nabla\phi = \vec{c}$, the diffraction pattern is rigidly shifted across the detector, with deflection angle $\beta \propto |\nabla\phi|$. (c) When $\nabla\phi$ varies across the width of the probe, the diffraction pattern intensity is not simply rigidly shifted, but rather redistributed across the detector in a more complex manner.

where $\otimes$ denotes convolution, $\mathcal{F}$ denotes Fourier transform with respect to x and y, and k_x and k_y are the corresponding Fourier-space coordinates. If there is no phase gradient within the sample, the whole probe wave function experiences the same phase shift, and no discernible change is made to the intensity profile at the detector. This is illustrated in Fig. 1(a). Alternatively, if there is a constant phase gradient across the width of the probe, the detected intensity will be rigidly shifted in the detector plane (as per the Fourier-shift theorem) and this intensity shift can be measured through the difference in signal between the different segments in a laterally divided detector [14,19–21]. This is illustrated in Fig. 1(b). However, the lateral variation in the phase gradient of the specimen may be on a scale smaller than that of the probe. In this case, the intensity redistribution on the detector will not be simply a rigid shift, but a more complex rearrangement, as indicated in Fig. 1(c) [16,21,22].

Quantitative interpretation of rigid-intensity shifts is possible with two or more detector segments [14,23]. Quantitative interpretation of the more complex intensity redistribution is feasible—via several possible routes including center-of-mass analyses and ptychography [16,20,24]—but each of these require a significantly higher sampling in the detector plane (up to $\sim 1024^2$ thus making much higher demands of experimental equipment) and a more involved analysis process. Thus, we seek to develop a framework to clarify when the simpler rigid-disk-shift interpretation is likely to be quantitatively accurate and when more complex data collection and analysis is required. We also propose beam-shaping strategies to broaden the range of experiments for which the rigid-disk-shift model can be applied.

This paper is organized as follows. In Sec. II, a review is made of idealized Airy probes and their broad tail intensities. In Sec. III, a p-n junction in a gallium arsenide (GaAs) specimen is explored as a case study of a phase profile varying in one dimension (i.e., $\nabla\phi$ is a function of x alone), using both experimental data and an analytical model to investigate realistic limits to the rigid-disk-shift model of scanning-probe DPC. A simulation study of magnetic diamond domains in a nickel-iron (NiFe) specimen is explored as a case study of a two-dimensional (2D)-varying phase profile in Sec. IV. Though these examples are drawn from electron microscopy imaging of nanoscale fields, the conclusions apply equally to imaging one-dimensional (1D)- and 2D-varying strong phase objects with similar proportions between sample feature and probe sizes with any probe quanta. These case studies demonstrate that while the rigid-intensity-shift model does not hold exactly, for imaging long-range fields the more complex intensity redistribution occurs predominantly near the edges of the diffraction pattern. As such, Sec. V explores the precision obtainable for quantitative field imaging with a segmented detector when analyzed in the rigid-intensity-shift model. Since the extent of probe tails is shown to be a limiting factor, Sec. VI proposes a beam shaping strategy to extend the validity of the rigid-intensity-shift model.

II. PROBE SHAPE EFFECTS

A requirement for the rigid-disk-shift model to be exact is that the phase gradient is linear across the full width of the probe. This is a rather stringent requirement, when considering the idealized probe in many DPC settings is formed from a plane-wave illuminated sharp aperture, in the far pre-field of the specimen (and thus necessarily has broad tails in the sample plane).

An ideal, circular aperture illuminated with planar illumination will form a focused probe in the far field:

$$|\Psi_{\text{entrance}}(x,y)|^2 = I_0\left[\frac{J_1(2\pi k_0\alpha r)}{2\pi k_0\alpha r}\right]^2, \tag{3}$$

where I_0 is an intensity normalization, $r = \sqrt{x^2+y^2}$, J_1 is a first-order Bessel function of the first kind, and $k_0 = 1/\lambda$. Such a probe is well known, comprising a central Airy disk surrounded by weaker rings with intensities decreasing slowly with radius. This is shown as an intensity profile in Fig. 2(a). In coherent probe imaging, the probe size is typically referred to as $r_{\text{probe}} = 0.61\,\lambda/\alpha$, the radius of the central disk. However, as shown in the enclosed intensity plotted in Fig. 2(b), this central disk contains only 84% of the probe intensity. The remaining intensity is broadly distributed, as demonstrated by comparison with a Gaussian probe of the same full width at half maximum (FWHM) [25,26]. If instead we define the probe radius as $r_{95} = 1.96\,\lambda/\alpha$, the radius which contains 95% of the probe intensity, the potential for inaccurate data interpretation in scanning-probe DPC becomes clear: the probe has a much larger spatial extent in real space than is typically accounted for.

In this paper we seek to better understand the diffraction pattern intensity redistribution in objects with long-range fields, to establish the domain of validity of the rigid-intensity-shift

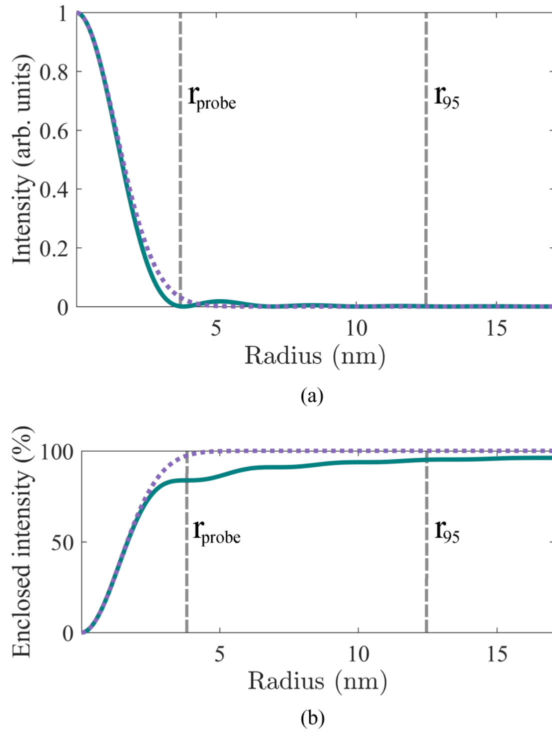

FIG. 2. (a) Comparison of Airy (teal, solid) and Gaussian (lilac, dashed) intensity profiles. (b) Comparison of enclosed energy for the Airy and Gaussian probes. These plots assume $2\pi k_0\alpha = 1\ \text{nm}^{-1}$; for suitable scaling via Eq. (3) these distributions can apply to any k_0 and α combination.

model of scanning-probe DPC, and to explore the manner in which it breaks down.[1]

III. 1D-VARYING PHASE PROFILE CASE STUDY: p-n JUNCTION IN GaAs

For our initial analytic modeling, we desire a system with a well-defined phase profile that varies in only one dimension. For these reasons, we revisit and extend a previously examined case of a p-n junction (290-nm-thick specimen of GaAs, with a symmetrical p-n junction between 10^{19}cm^{-3} p-doped (Zn) and $10^{19}\ \text{cm}^{-3}$ n-doped (Si) regions [17,29]). In this system, the transmission function describing the phase profile imparted by the intrinsic electric field across the junction is well approximated by the 1D function [29]:

$$T_{p-n}(x) = \exp\left[i\chi \operatorname{erf}\left(\frac{x}{d}\right)\right], \tag{4}$$

where for our case study $\chi = 0.879$, making this a strong phase object, and the characteristic width of the junction is $d = 17$ nm. The former value follows from $\chi = \sigma t V_0$ and these material parameters: σ, the interaction constant (7.29×10^{-3} (V nm)$^{-1}$ for 200 keV electrons) [30]; $t = 67$ nm, the (deduced) active-region thickness; and $V_0 = 1.8$ eV, the difference in mean inner potential between the p- and n-doped regions of the semiconductor material. The numerical values pertinent to this specimen were determined in Ref. [29]. Note that a similar model can be used to describe the complex transmission function for unpolarized x rays, neutrons, and visible light traversing a diffused gradient between two transparent media, or an interface between volumes having two different densities of the same material.

In seeking to understand the limits of the rigid-disk-shift model, we illuminated this specimen with three different probe sizes, characterized by convergence semiangles $\alpha = 133$, 426, and 852 μrad, the scaling of which is shown in comparison to that of the phase profile of the transmission function of the junction in Figs. 3(a), 3(b), and 3(c), respectively.[2] The $\alpha = 133\ \mu$rad case produces the broadest probe, and is that used previously [17,29] for which the diffraction pattern showed an intensity redistribution more complex than a simple rigid-intensity shift. This followed because the widths of the p-n junction and probe intensity distribution are comparable: The phase gradient varies appreciably across the central intensity lobe of the probe distribution, as seen in Fig. 3(a). We might therefore expect that the finer probes, for which Figs. 3(b) and 3(c) show less variation in the phase gradient across the region of appreciable intensity, would better justify the rigid-disk-shift model. This expectation is reinforced by the DPC-STEM profiles in Fig. 3(d) which converge to essentially the same profile for the two narrower probes.

The detailed diffraction pattern distributions, however, show that the scattering physics is not so simple. Figure 4 compares diffraction patterns between experiment and simulation [using Eq. (2)] for the three different convergence semiangles. The intensity profiles, taken from across the center of the full diffraction patterns, compare on-junction to off-junction results. The experimental and simulated patterns are in broad qualitative agreement. (The Fresnel fringing and other fine structure evident in the experimental patterns result from the images having been recorded on photographic film and so containing residual aberrations that were not able to be identified and minimized during recording.) A rigid-disk-shift model would predict a shift of approximately 18 μrad (based on the field strength at the center of the junction), but the patterns make clear that none of the on-junction patterns are simply rigidly shifted versions of their off-junction counterparts. Rather, each pattern shows a bright-intensity peak on the right-hand edge of the disk, and a reduced-intensity

[1] Chapman *et al.* [27] explored this question in the context of domain wall imaging by Taylor expanding the imparted phase of Eq. (1) to second order in x and assuming the second order term was adequately described by the weak phase approximation. Appropriate to the instrumentation of the time, the first order correction to the rigid-shift model depended on lens aberrations but vanishes in an aberration-free system. The current generation of aberration corrected STEM instruments offer greater control over lens aberrations, and a particular strength of DPC-STEM is that it can be done in-focus, usually the optimum imaging conditions for other STEM imaging modes (such as high-angle annular dark-field [28]) that one might wish to acquire simultaneously [18,29].

[2] In contrast to Fig. 2, the probe amplitude, $|\Psi_{\text{entrance}}|$, is shown here to emphasise the extent of the probe tails.

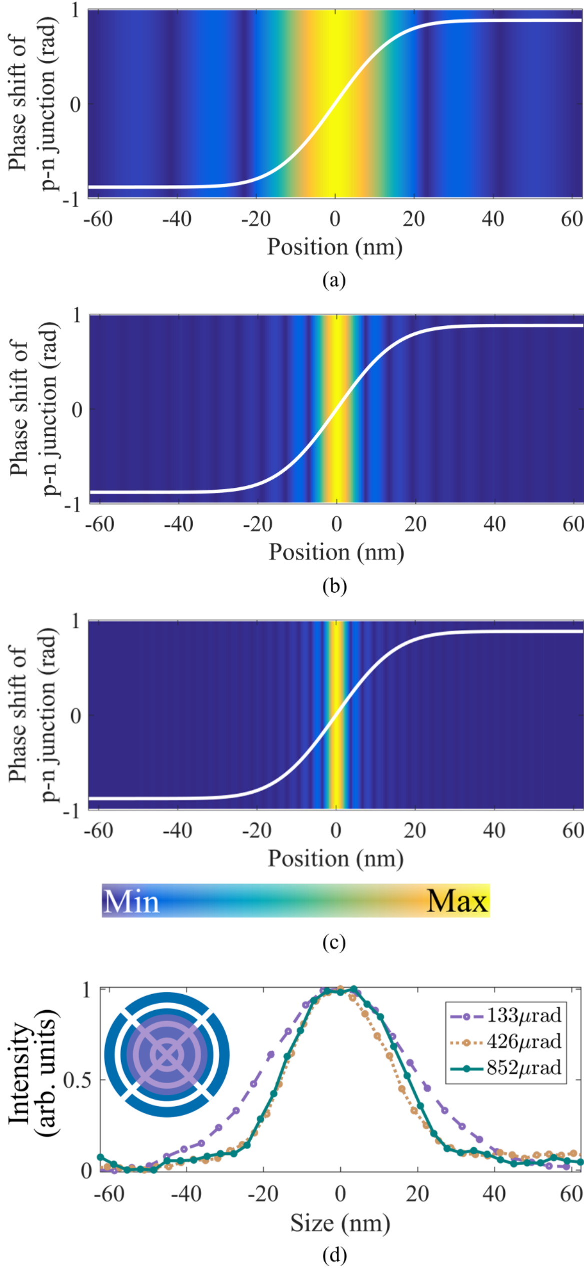

FIG. 3. Plots of the p-n junction phase profile, underlaid by a color map of the probe amplitude profile, extended vertically to aid visual comparison between the variation in curvature of the junction phase profile and spatial extent of the probe amplitude profile, for the probe-forming aperture semiangles (a) $\alpha = 133$ μrad, (b) $\alpha = 426$ μrad, and (c) $\alpha = 852$ μrad. (d) Experimental p-n junction DPC-STEM profiles as imaged with the three different probes. These profiles were obtained by taking the difference between the STEM images from two diametrically opposed detector segments (depicted in the figure inset) under the edges of the bright field disk and integrating the result along the length of the junction.

trough on the left-hand edge of the disk, at diffraction-plane positions broadly within the same area as that illuminated in the off-junction case. Indeed, although these peak and trough features constitute a smaller fraction of the diffraction pattern for increasing the convergence semiangle, their angular extent is the same in each case.

To better understand these features, let us consider a piecewise approximation to Eq. (4) that is amenable to analytic manipulation. Assuming a constant electric field within the p-n junction and zero electric field outside, the transmission function may be written:

$$T(x) = \begin{cases} e^{-i\varphi D/2} & x < -D/2 \\ e^{i\varphi x} & |x| \leqslant D/2 \\ e^{i\varphi D/2} & x > D/2 \end{cases}, \tag{5}$$

where D is the nominal width of the junction and $\varphi = \sigma V_0 t/D$. Note that D is different from the characteristic width d in the error function model of Eq. (4). For $d = 17$ nm, a value of $D = 46$ nm minimizes the root-mean-square error between this piecewise approximation and the error function model, the comparison is shown in Fig. 5(a)-i.

Equation (5) can be rewritten in terms of functions commonly found in tables of Fourier transforms:

$$\begin{aligned} T(x) =& \cos(\varphi D/2)[1 - \mathrm{Rect}_D(x)] \\ &+ i\frac{\sin(\varphi D/2)}{2}[\delta(x - D/2) + \delta(x + D/2)] \otimes \mathrm{sgn}(x) \\ &+ e^{i\varphi x}\mathrm{Rect}_D(x), \end{aligned} \tag{6}$$

where $\mathrm{sgn}(\pm|x|) = \pm 1$ is the sign function and $\mathrm{Rect}_D(x)$ is the rectangle function given by

$$\mathrm{Rect}_D(x) = \begin{cases} 1 & |x| < D/2 \\ 0 & \text{otherwise} \end{cases}. \tag{7}$$

The first two terms in Eq. (6) are only nonzero for $|x| \geqslant D/2$ and so pertain to the field-free region of the specimen. The final term is only nonzero for $|x| < D/2$ and so pertains to the region of the specimen where the electric field is constant. Fourier transformation of Eq. (6) gives

$$\begin{aligned} T(k) =& \cos(\varphi D/2)[\delta(k) - D\,\mathrm{sinc}(\pi Dk)] \\ &+ \frac{\sin(\varphi D/2)\cos(\pi Dk)}{\pi k} + D\,\mathrm{sinc}[\pi D(k - \varphi/2\pi)]. \end{aligned} \tag{8}$$

With reference to Eq. (2), the diffraction plane wave function of the scattered probe is given by the convolution of Eq. (8) with the reciprocal space illumination wave function (the aperture function). In one dimension, the aperture function is a top hat and, for comparison with the experiments, we have set the width to be $\alpha = 133$ μrad. The resulting diffraction pattern is shown in Fig. 5(a)-ii as a teal, solid line. For reference, the reciprocal-space form of the entrance wave function intensity $|\Psi_{\mathrm{entrance}}|^2$, the aperture function, is also shown as a lilac, dotted line. It can be seen that the simplified analytic model qualitatively accounts for the features of the diffraction pattern plotted in Fig. 4 for the $\alpha = 133$ μrad case, which used the error function model for the phase of the p-n junction transmission function. Different components of Eq. (8) are plotted in Fig. 5(a)-iii. Before discussing these in detail, it is helpful to consider two limiting cases.

The third term in Eq. (8), $D\,\mathrm{sinc}[\pi D(k - \varphi/2\pi)]$, corresponds to the region of constant electric field in Eq. (5) and

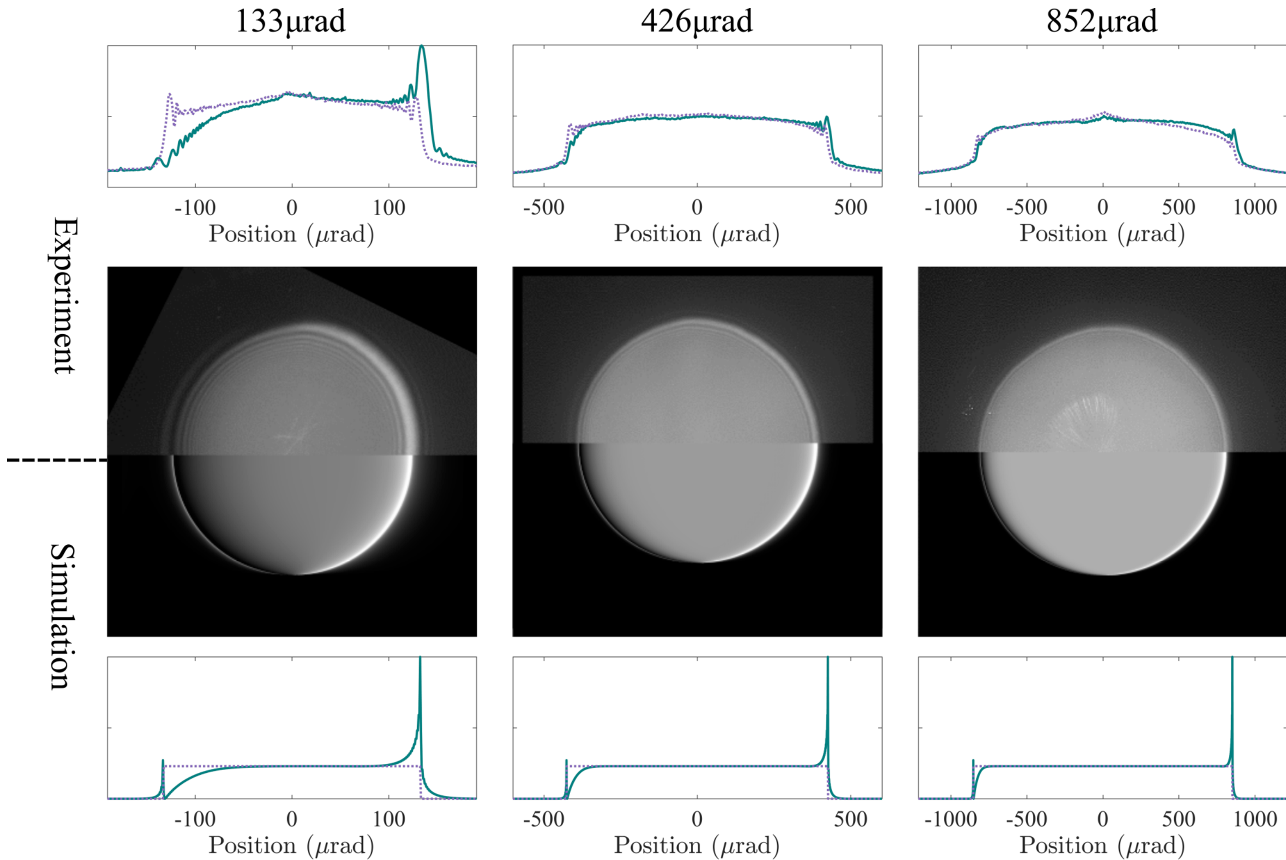

FIG. 4. Line profiles and 2D diffraction patterns comparing experiment and simulation for three different convergence semiangles, illuminating the p-n junction specimen. The line profiles compare results on-junction (teal, solid) with those off-junction (lilac, dashed).

accounts for a shift in the diffraction pattern center of mass due to the transverse electric field of the specimen. In the limit $D \gg 1$, this sinc term will approach a δ function (i.e., cause a rigid shift of the illumination). Figure 5(b)-i plots the transmission function phase assuming the limiting case of a very large p-n junction with the same built-in electric field ($|\nabla\phi| = 3.68\times10^{-2}$ rad/nm). This causes the diffraction pattern to shift rigidly to the right (by 5.83×10^{-3} nm^{-1} or 14.6 μrad), as shown in Fig. 5(b)-ii. The Fourier transform of the transmission function is seen to essentially be a δ function, Fig. 5(b)-iii.

In the limit $D \to 0$, but with φ scaled such that φD is constant, Eq. (8) approaches

$$T(k) = \cos(\varphi D/2)\delta(k) + \frac{\sin(\varphi D/2)}{\pi k}. \tag{9}$$

Here it is possible to derive an analytic expression for the diffraction pattern:

$$|\Psi(k)|^2 = \frac{1}{2\alpha k_0}\left[\cos(\varphi D/2)\mathrm{Rect}_{\alpha k_0}(k) + \frac{\sin(\varphi D/2)}{\pi}\ln\left|\frac{k+\alpha k_0}{k-\alpha k_0}\right|\right]^2. \tag{10}$$

Setting $\varphi D = 1.76$ rad, to produce the same potential difference as that across the p-n junction in Fig. 5(a)-i, gives the step-function transmission function phase shown in Fig. 5(c)-i. The diffraction pattern resulting from Eq. (10) is plotted in Fig. 5(c)-ii. The most pronounced features in this diffraction pattern are the sharp peaks at $k = \pm\alpha k_0$, i.e., at the edges of the aperture function, resulting from the logarithmic divergence in Eq. (10). Note that α is the only meaningful length scale in this limit, and as such the intensity both within and spreading beyond the aperture function varies on this scale. Figure 5(c)-iii plots the transmission function $T(k)$, showing the divergence inherent in the $1/k$ factor in the second term of Eq. (9). This establishes why the points of divergence in the diffraction pattern occur at the edges of the aperture function: In convolving the top-hat function with this transmission function, those are the points where the top hat overlaps only one-half of the $k \to 0$ divergence.

Figure 5(b) and the associated discussion showed how the sinc term in Eq. (8) gives rigid-intensity-shift behavior. Similarly, Fig. 5(c) and the associated discussion showed how the $1/k$ term in Eq. (8) leads to the sharp peaks at the edges of the aperture function. These observations aid interpretation of the relative contribution of the different terms in Eq. (8) to the diffraction pattern shown in Fig. 5(a)-ii resulting from the piecewise approximate p-n junction potential. Figure 5(a)-iii explores the relative contributions of the second and third term in Eq. (8). The transmission function $T(k)$ is plotted as a teal, solid line; the second term, $\sin(\varphi D/2)\cos(\pi Dk)/\pi k$, as a lilac,

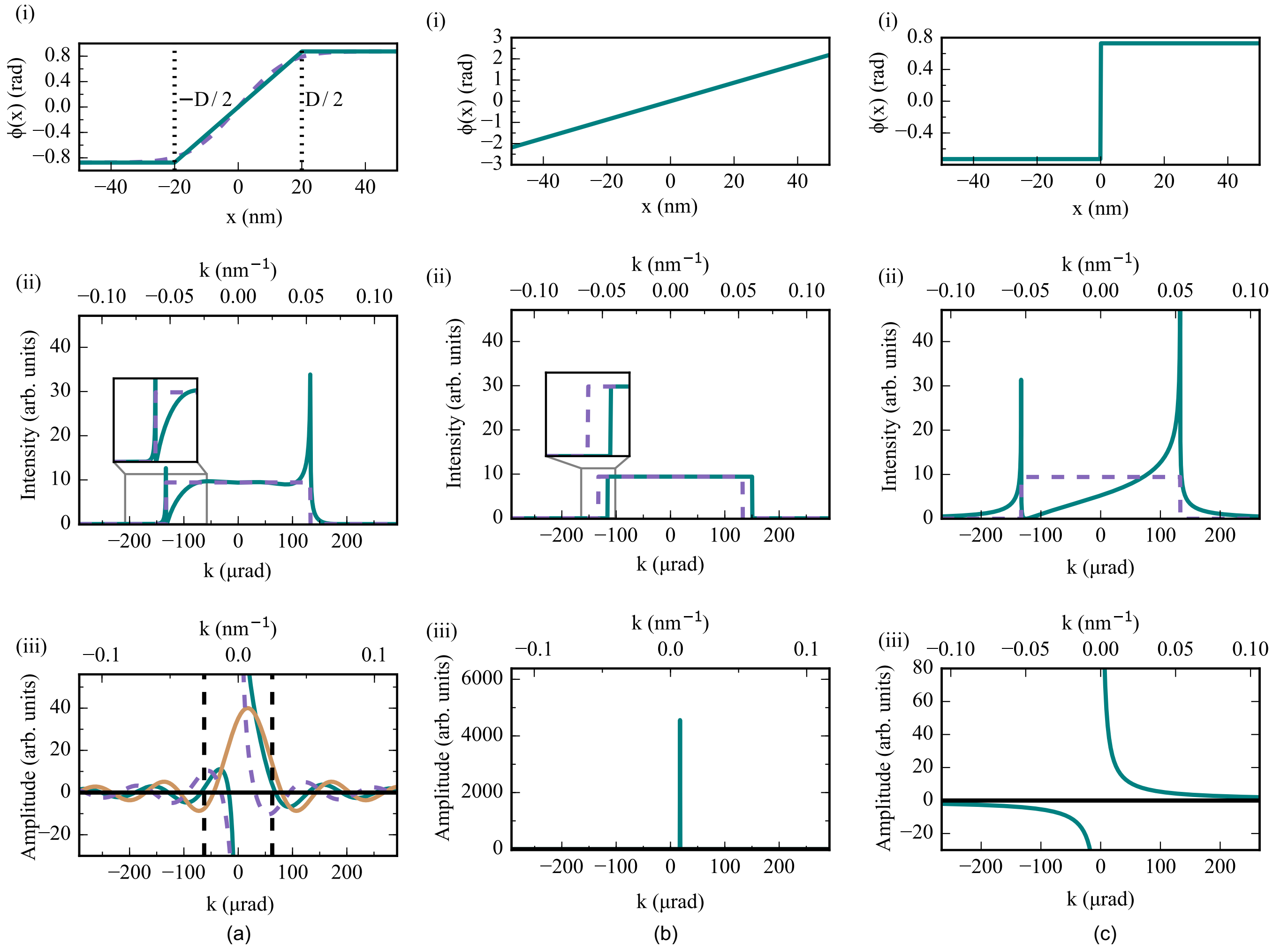

FIG. 5. For (a) the piecewise p-n junction model of Eq. (5), (b) the $D \to \infty$ limit, and (c) the $D \to 0$ limit we plot the (i) real-space transmission function phase, (ii) diffraction pattern, and (iii) reciprocal-space transmission function. In (a)-i the piecewise p-n junction model phase (teal, solid), is compared to the continuous equivalent function (lilac, dashed). In parts (ii), the diffraction pattern on-junction (teal, solid) is compared to that off-junction (lilac, dashed). In (a)-iii the reciprocal-space transmission function (teal, solid) is compared to the second term of Eq. (8) (lilac, dashed) and the third term of Eq. (8) (mustard, solid), with vertical black lines positioned at $\pm 1/D$ as guides to the eye.

dashed line; and the third term, the sinc term, as the mustard, solid line.

It can be seen that $T(k) \to \pm\infty$ as $k \to 0$ due to the $1/k$ factor in the second term in Eq. (8), which necessarily dominates for sufficiently small k and, as seen in discussion of Fig. 5(c), leads to sharp intensity peaks at the edges of the aperture function in Fig. 5(a)-ii, again the dominant feature of the diffraction pattern. Note, however, that there is now an additional length scale in the problem: the junction width D. Through the $\cos(\pi Dk)$ factor in the second term in Eq. (8), this has the effect of making the intensity peaks at the edges of the aperture function in Fig. 5(a)-ii narrower than those of Fig. 5(c)-ii.

While in the $D \to \infty$ limit in Fig. 5(b)-iii the sinc term containing the rigid-shift tendency was both δ-function-like and dominant, in Fig. 5(a)-iii it has finite width (of order $1/D$) and the shift of the central peak is hidden within the divergence of the $\sin(\varphi D/2)\cos(\pi Dk)/\pi k$ term. The former means that the width of the intensity variation in the extended peak-trough feature is about $1/D = 0.025$ nm^{-1}, or about 60 μrad, consistent with Fig. 5(a)-ii. The latter means that the shift of the diffraction pattern intensity is obscured by the peak-trough feature.

It is also instructive to consider a case where the rigid-disk-shift model is known to be a good approximation. Krajnak shows model data from a polycrystalline magnetic sample which imposes a linear phase gradient of $\nabla\phi = 0.073$ rad/nm on the wave function in a region that extends for 200 nm, which is much larger than the probe ($r_{95} = 11.3$ nm for a 436 μrad probe forming aperture at 200 keV) [31]. Figure 6(a) is the same as Fig. 5(a)-i except that parameters pertinent to the Krajnak model have been used. As can be seen in Fig. 6(b), especially in the magnified inset, the intensity distribution in the diffraction pattern is rather well described by the rigid-disk-shift model, though on close inspection small intensity peaks at the edge of the aperture function are still evident.

We can understand this qualitative difference from Fig. 6(c), which explores the relative contributions of the second and

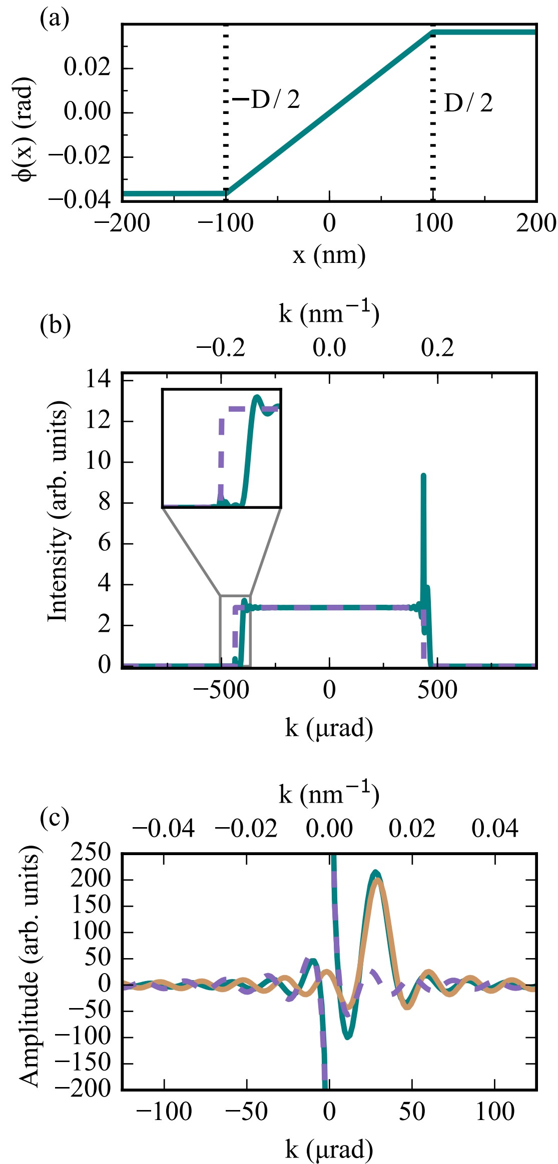

FIG. 6. (a) Real-space transmission function phase, (b) diffraction pattern, and (c) the reciprocal-space transmission function for the piecewise object of Eq. (5) for parameters taken for a transmission function of a magnetic domain taken from Ref. [31]. The line styles are as per Fig. 5(a). Note that (b) and (c) are plotted with different horizontal scales, because the features in (b) are an order of magnitude smaller than those in Fig. 5(a)-ii.

third term in Eq. (8). Again, $T(k) \rightarrow \pm\infty$ as $k \rightarrow 0$ because the $1/k$ factor in the second term necessarily dominates for sufficiently small k, explaining the small intensity peaks at the edge of the aperture function. Note, however, that these terms are smaller and narrower than the intensity peaks in Fig. 5(a)-ii because the $\cos(\pi Dk)$ factor in the second term oscillates rapidly (due to the large value of D).[3] It is likely that such oscillations would be challenging to observe experimentally, even on state-of-the-art instruments, due to finite beam coherence and detector resolution, and further complicated by such oscillations being similar in form to Fresnel fringes resulting from imperfect focusing. Also in contrast to Fig. 5(a)-iii, the sinc term containing the rigid-shift tendency is much narrower (because $1/D$ is smaller) and is clearly separated from the divergence point of the second term. That the magnitude of the shift in k is larger than the $1/D$ length scale on which the diffraction pattern intensity varies means that there is now a dominating shift of the diffraction pattern intensity.

The shift, $\varphi/2\pi = |\nabla\phi|/2\pi$, in the third term in Eq. (8) will be greater than the $1/D$ length scale on which the diffraction pattern intensity varies if

$$\frac{|\nabla\phi|}{2\pi} D > 1\,. \tag{11}$$

Noting that in the ideal rigid-disk-shift case the detected deflection angle β can be related to the imparted phase gradient (for small deflections) via [23,31]

$$|\nabla\phi| = 2\pi k_0 \beta, \tag{12}$$

Eq. (11) can also be written as

$$\beta > \frac{1/D}{k_0} \equiv \gamma, \tag{13}$$

where γ is the scattering angle scale of the intensity redistribution at the edge of the diffraction patterns. It is also interesting to note that recognizing the mean momentum transfer to the probe as $\Delta p = h\Delta k \approx h|\nabla\phi|/2\pi = \hbar|\nabla\phi|$ and the size of the junction as $\Delta x = D$, then Eq. (11) becomes analogous to the quantum mechanical Heisenberg uncertainty principle:

$$\Delta p \Delta x > h. \tag{14}$$

By comparing the size of the different probes against the p-n junction in Fig. 3 we anticipated that, while the phase gradient varied appreciably on the scale of the $\alpha = 133\,\mu$rad probe, the much narrower $\alpha = 852\,\mu$rad probe would have shown a more rigid-intensity-shift-like behavior. However, this was not supported by the experimental and simulated results in Fig. 4. The additional conditions of Eqs. (11) and (13) explain this: The deflection expected from the peak field strength in the p-n junction is $\beta \approx 18\,\mu$rad, which is smaller than the length scale on which the diffraction pattern intensity varies, $\gamma \approx 60\,\mu$rad. This requirement is fundamental to the object but independent of the probe forming aperture, which is why forming a finer probe failed to make the scattering more rigid-shift-like in Fig. 4. Conversely, in the Krajnak example, $\beta \approx 29\,\mu$rad is appreciably larger than $\gamma \approx 13\mu$rad, hence the rigid-intensity-shift model holds better.

We now seek to broaden our understanding through a study of a more complex specimen geometry where $\nabla\phi$ varies in both x and y.

[3] These rapid oscillations might also be considered an example of the well-known Gibbs phenomenon [19] where if even a generous bandwidth limit is applied to a step discontinuity then high frequency oscillations will result near the discontinuity. Here, the $\mathrm{Rect}_D(x)$ factor in the transmission function in Eq. (6) acts as a bandwidth limit on the shifted component of the probe.

IV. 2D-VARYING PHASE PROFILE CASE STUDY: MAGNETIC DOMAINS IN NiFe

DPC-STEM has been particularly useful for studying magnetic microstructure [32–35]. As such, phase gradients imposed by magnetic domains are a highly relevant model system. Here we work with a simulated specimen of NiFe, with magnetization vectors generated using the Object Oriented MicroMagnetic Framework (OOMMF) software developed at the National Institute of Standards and Technology (NIST) [36]. A standard soft magnetic material was modeled using the anisotropy constant $K = 0\ \mathrm{J/m^3}$, saturation magnetization $M_s = 860\ \mathrm{kA/m}$, and exchange coefficient $A = 13\ \mathrm{pJ/m}$.

The magnetization vectors were converted to transmission function phase shifts following Refs. [9,37], and interpolated to match the real-space requirements for adequately sampled STEM diffraction calculations. The electric potential is assumed constant. The phase distribution imparted by this structure is illustrated in Fig. 7(a), showing this to be a strong phase object. The crosses indicate the probe positions at which the diffraction patterns shown in Fig. 7(b) were calculated, assuming a 133 μrad convergence semiangle.

In these diffraction patterns, a number of features are visible. Diffraction patterns (i) and (iii) both show the diagonal symmetry of the phase profile at their respective probe positions, but with more pronounced peak-trough features in (iii) as more of the probe is sitting over regions of nonconstant $\nabla\phi$. Diffraction patterns (ii), (iv), and (vii), with the least variation in phase gradient under the center of the probe, show a general trend of intensity shift from their central position, but are still decorated with substantial intensity redistributions. Figures 7(b)-v and 7(b)-ix are rather similar—the probe positions have the same local symmetry though the phase profiles have opposite signs. When $\nabla\phi$ varies dramatically under the central region of the probe, the intensity redistributions of the diffraction pattern become more pronounced.

The diffraction patterns in Fig. 7(b) show sharp peak-trough-type features not unlike those seen earlier in Fig. 4: Such features are not exclusive to the simple 1D-varying phase profile case but rather occur over a variety of systems and probe positions. The generality of these features means that the rigid-intensity-shift model will rarely be exactly realized. If the diffraction patterns in Fig. 7(b) were recorded on a pixel detector, the deviation from the rigid-intensity-shift model might itself be used to extract information about the structure. If instead a segmented detector were used, the deviation from the rigid-intensity-shift model would be hard to gauge from the STEM images alone. However, this loss of sensitivity to fine intensity redistribution may not necessarily be a great limitation: If the intensity redistribution is sufficiently localized within the detector segments then a rigid-intensity-shift analysis applied to segmented detector DPC-STEM may be a good approximation. To explore this, we now compare the true phase gradient of Fig. 7(a) with that estimated by a segmented detector.

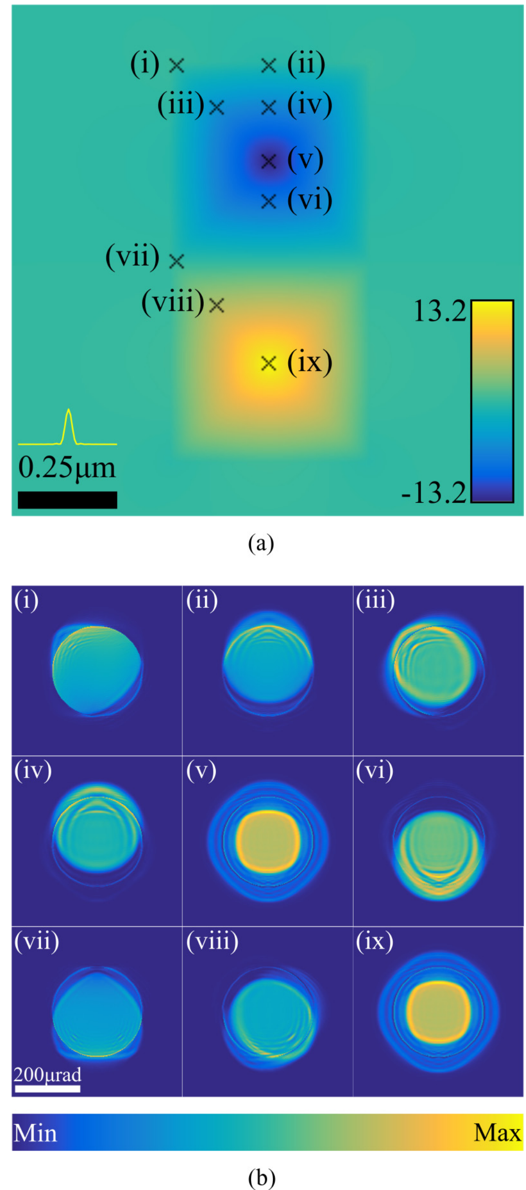

FIG. 7. (a) Phase profile imposed by the magnetized specimen (1 μm × 0.5 μm), with color bar in radians. The crosses mark the probe positions for which the diffraction patterns in (b) are calculated, assuming a 133 μrad probe [the intensity profile of which is plotted above the scale bar in (a)]. The intensity scale for each diffraction pattern has been set independently to better visualize the fine structure therein.

V. EFFECT OF INTENSITY REDISTRIBUTIONS ON SEGMENTED DETECTOR DPC-STEM ACCURACY

Assuming a rigid-disk-shift model, segmented detector STEM images can be used for quantitative phase gradient measurement via a calibration establishing the correspondence between the signal in the various detectors and the magnitude and direction of the disk deflection. Majert and Kohl [38] present analytic expressions for deflected bright-field disk overlap with detector segments while Zweck *et al.* used its analytical tractability to establish clear guidelines for achievable field sensitivity [23,39]. Alternatively, the calibration can be carried out experimentally [17,23,29,39], which has the advantage of accounting for the realistic detector response and some spreading of the bright-field disk via inelastic scattering.

Our simulations were set up as follows. To emulate the experimental setup used to obtain Fig. 3(d), the detector was

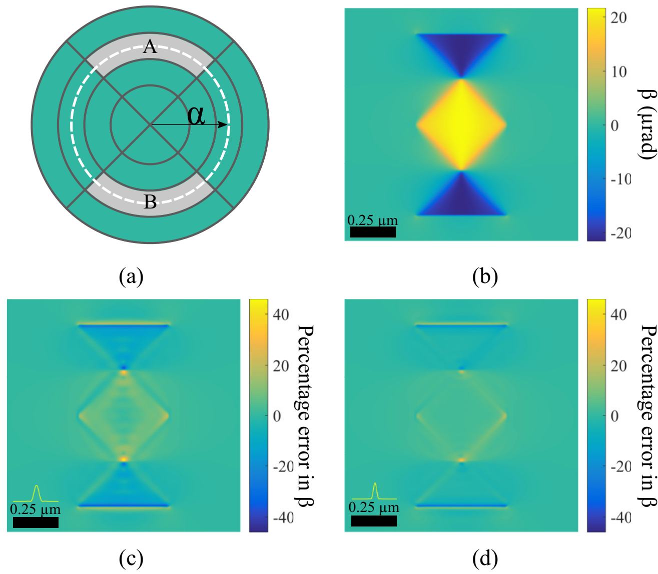

FIG. 8. (a) Illustration of location of the edges of the off-sample bright-field disk (white, dashed line) compared to the segmented detector. (b) $\partial\phi/\partial y$ of the phase profile in Fig. 7. Color bar is in terms of the probe deflection angle β in μrad. Difference between the calibrated segmented detector DPC-STEM estimate for $\partial\phi/\partial y$ and the true value for convergence semiangles of (c) 90 μrad and (d) 133 μrad, with the corresponding probe intensity profiles plotted to scale in the lower left corners. Color bars for (c) and (d) given in terms of percentage error from maximum β in (b).

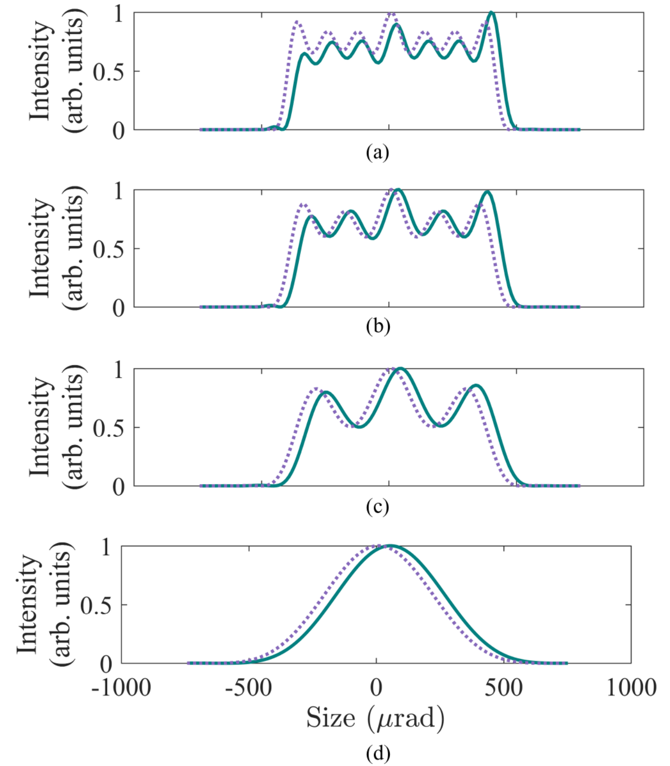

FIG. 9. Line profiles of diffraction intensity from 426 μrad convergence semiangle Airy probes apodized at the (a) seventh, (b) fifth, (c) third, and (d) first radial minimum, for the probe off (lilac, dashed) and on (teal, solid) the p-n junction described by Eq. (4).

oriented as indicated in Fig. 8(a), with camera length chosen such that the bright-field disk extends to midway through the third ring of detector segments. To calibrate phase measurements of $\partial\phi/\partial y$, for each convergence semiangle considered a look-up table was generated relating the difference in intensity recorded in segment A and segment B [see Fig. 8(a)] to the actual bright-field disk shift. Note that a more elaborate approach, perhaps based on approximate center of mass, would be needed to handle deflections which shift the bright-field disk completely off either of segment A or B. Figure 8(b) shows $\partial\phi/\partial y$ for the magnetic domain structure of Fig. 7(a). For convergence semiangles of 90 μrad and 133 μrad, respectively, Figs. 8(c) and 8(d) show the difference between the calibrated segmented detector DPC-STEM estimate for $\partial\phi/\partial y$ and the true value.

The segmented detector measurement of the phase gradient is least accurate near regions of phase gradient change (most significantly at the top and bottom edges of the sample). However, in Fig. 8(c) further differences are perceptible as more subtle ripples lying horizontally across the domains in the difference image. These are regions where the true phase gradient is linear, but peaks and troughs in the diffraction patterns pass on and off the detector segments, as a result of the broad probe tails. The dynamics of this rippling behavior are shown in more detail in Supplemental Material [40].

In Fig. 8(d), the differences are more localized to regions of strong phase gradient change. As previously seen in Fig. 4, changing the convergence semiangle does not necessarily alter the angular extent of the intensity redistribution at the edges of the bright-field disk. However, because we assume camera lengths such as to maintain the same geometric overlap between the detector segments and the bright-field disk, as the convergence semiangle increases the intensity redistribution on the edges of the bright-field disk becomes more localized with respect to the detector segments. This is shown in Supplemental Material [40].

Figures 8(c) and 8(d) show the typical error is of the order of 10% of the signal. The largest errors are strongly localized to specific features. For most of the imaged area the errors remain small: segmented detector DPC-STEM can give good quantitative results even when, as shown in Secs. III and IV, there are significant deviations away from a rigid-disk shift.

VI. EFFECT OF PROBE SHAPING ON SEGMENTED DETECTOR DPC-STEM ACCURACY

The analytic modeling in Sec. III and the ripples in the difference map in Fig. 8(c) suggest that much of the remaining discrepancies are attributable to the long probe tails. It follows that if the interrogating probe can be reshaped to minimize the breadth and intensity of the probe tails then the accuracy of quantitative segmented detector DPC-STEM would improve further still.

Novel electron probe shaping has become feasible over the last few years, primarily in conjunction with studies into electron vortex beams [41–45]. A number of routes to shape electron probes were developed, including manipulating optical aberrations [46,47], exploiting the mean inner potential of materials [48,49], and using nanoscale magnetic fields [50,51].

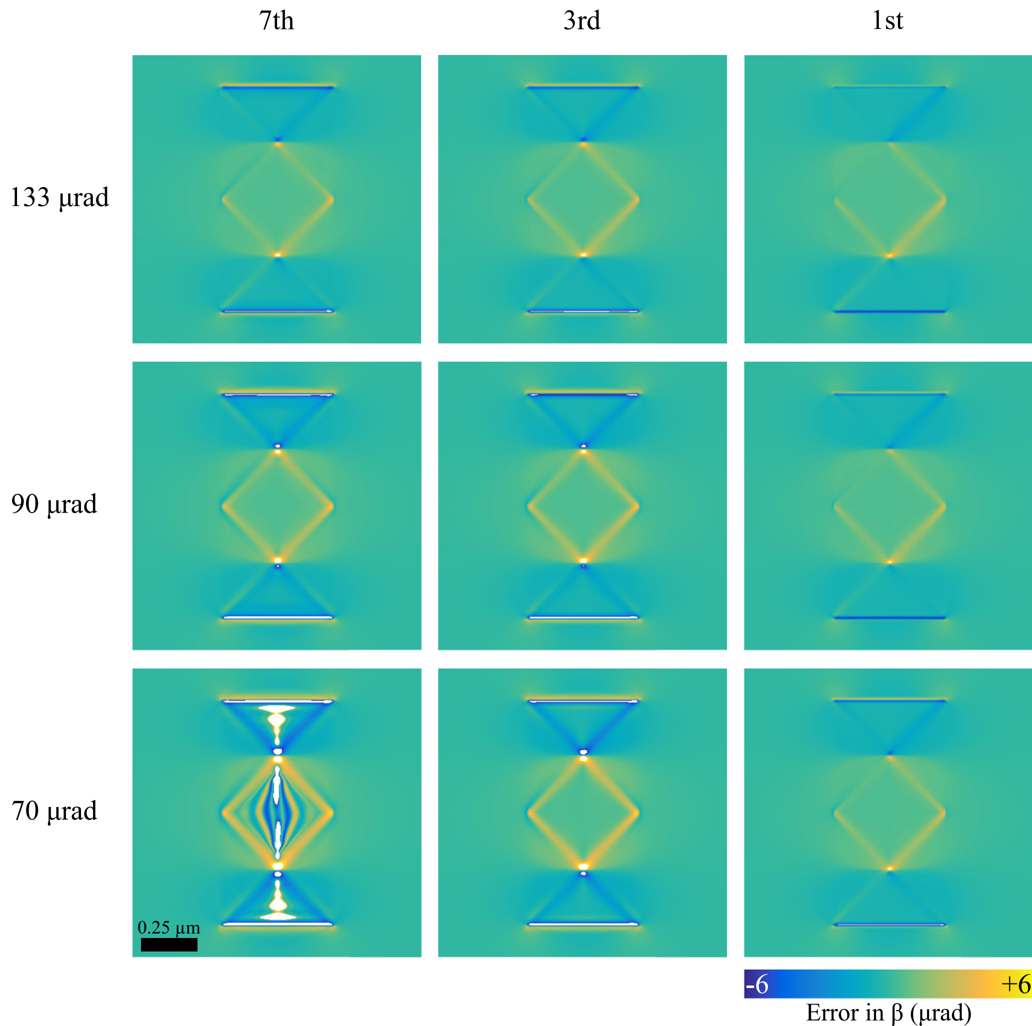

FIG. 10. Difference maps in deflection angle between the true phase gradient and that calculated with the look-up table, for different α (rows) and apodization (columns). The differences decrease with increasing α, as expected, but decrease more strongly with increasingly narrow apodization, the first Airy apodization cases (right-hand column) all giving similar difference measurements. The color maps are restricted to ± 6 μrad to visualize the details more clearly. Difference values outside this range have been set to white.

In particular, as it is now possible to produce probes that do not have the long probe tails of the Airy probe, we investigate the effect of reduced probe tail width on the quantitative accuracy of segmented detector DPC-STEM.

A simple probe shape with reduced tail intensity is a Gaussian probe; cf. Fig. 2. The literature gives two different routes to creating such a probe. Recent work by McMorran *et al.* has used electron phase plates to form a Gaussian wave front directly [52]. A less elegant method—but one perhaps simpler to employ since such phase plates are not yet widely available and inserting them into electron microscopes is nontrivial—would be to use judicious combinations of the several condenser apertures typically available in the microscope. A first condenser aperture would create the standard Airy-disk electron probe, and a later (but still pre-sample) aperture could be used to truncate the probe at a minimum of the Airy disk. Such probe truncation (as a simple example of apodization) is well known in astronomy and visible light optics and can produce a good approximation to a Gaussian beam [25,53].

We return to the p-n junction case, Eq. (4), to demonstrate the changes in the diffraction plane caused by successive apodizations of the Airy probe. Figure 9 shows simulated intensity profiles of the diffraction pattern when the probe illuminates the center of the p-n junction and is apodized at the seventh, fifth, third, and first Airy minima. As compared with the top-hat diffraction intensity profile of an unapodized probe, the increasingly narrow apodization is seen to make the profile more Gaussian (the expected form of the diffraction pattern of a Gaussian probe). In Fig. 9(a), left-right asymmetry within the diffraction pattern is evident, echoing much of the behavior of Fig. 4. The central position of the diffraction pattern intensity may be somewhat shifted, but the intensity redistribution between the off-junction and on-junction cases is not a simple rigid shift. However, as the apodization radius becomes increasingly narrow, the intensity redistribution within the disk decreases in significance, and the shift of the diffraction pattern becomes clearer—the behavior predicted by the initial rigid-disk-shift model. In Fig. 9(d), the on-junction intensity is a simple shifted version of the off-junction intensity.

To explore whether this probe shaping improves the accuracy of quantitative segmented detector DPC-STEM, we turn again to the magnetic domain case study of Secs. IV and V. Over a series of convergence semiangles (70 μrad, 90 μrad, and 133 μrad) and apodization cutoffs (at the seventh, third, and first Airy minima), segmented detector simulations were performed to find the phase gradients obtained. The difference between these measured and true phase gradients, depicted in Fig. 10, show increasing localization of the sample regions that are not accurately reconstructed—the tails have a decreasing effect as the apodization strength is increased.

The reconstructed phases for the probes apodized at the first Airy minimum closely match the true phase gradient, aside from when the probe is within r_{probe} of a strong change in the phase gradient. Reducing probe tails does indeed seem to be a promising way to improve the quantitative accuracy of segmented detector DPC-STEM.

VII. CONCLUSION

In this study, the break down of the rigid-intensity-shift model of scanning-probe DPC when the gradient of the imparted phase varies across the incident wave function, previously anticipated in principle and observed in atomic-resolution STEM imaging [16,21,22,54], has been explored in detail. Combining analytic modeling in a general transmission-probe imaging system, we have shown that the breaking of this model is quite generic, and occurs for a range of specimen and probe parameters. While our experimental and simulated case study examples centered upon nanoscale field mapping in electron microscopy, our conclusions are equally applicable to imaging of strong phase objects via scanning-probe DPC using x rays, visible light, and neutrons. It is worth stressing for the case of electrons that this occurs in simple phase objects; it does not require dynamical scattering.

Whether applying rigid-disk-shift interpretation is valid depends on the relationship between properties of the specimen, detector, and probe. Our conclusions can be summarized as follows.

(1) The diffraction pattern intensity redistribution will not be well described in detail by a rigid-disk-shift interpretation, irrespective of probe size, unless the product of the phase gradient and the length over which it is constant is sufficiently large [see Eq. (11)].

(2) If the convergence semiangle is sufficiently large compared to the feature size, the diffraction pattern intensity redistribution may nevertheless be confined within a detector segment, allowing an accurate, quantitative DPC reconstruction using the simple rigid-disk-shift model.

(3) As deviations from the rigid-disk-shift model are exacerbated by the broad tails of Airy probes, probe reshaping to reduce these tails can enable quantitative, accurate DPC reconstruction for a broader range of specimens.

If the diffraction patterns were recorded on a pixel detector, the breakdown of the rigid-intensity-shift model is not particularly problematic and may even be used to extract information about the structure. However, that approach produces enormous data sets (on the order of $\sim 1024 \times 1024$ data points per probe position) and requires complicated analysis. Our results show that judicious use of convergence angle and probe shaping enables quantitative, accurate phase reconstruction to be achieved using DPC images recorded on just a few detector segments. This permits faster data collection and produces data files of easily manageable size, which is highly attractive for high-throughput practical applications.

ACKNOWLEDGMENTS

This research was supported by the Australian Research Council Discovery Projects funding scheme (Project No. DP160102338). N.S. acknowledges support from SENTAN, JST, and JSPS KAKENHI Grants No. JP26289234 and No. JP17H01316. The GaAs p-n junction samples were provided by Hirokazu Sasaki, Furukawa Electric Co., Ltd.

[1] F. Zernike, Science **121**, 345 (1955).

[2] R. Lewis, N. Yagi, M. Kitchen, M. Morgan, D. Paganin, K. Siu, K. Pavlov, I. Williams, K. Uesugi, M. Wallace *et al.*, Phys. Med. Biol. **50**, 5031 (2005).

[3] *Magnetic Imaging and Its Applications to Materials*, edited by M. De Graef and Y. Zhu (Elsevier, Amsterdam, 2000), Vol. 36.

[4] D. Paganin, S. Mayo, T. E. Gureyev, P. R. Miller, and S. W. Wilkins, J. Microsc. **206**, 33 (2002).

[5] B. Allman, P. McMahon, K. Nugent, D. Paganin, D. L. Jacobson, M. Arif, and S. Werner, Nature (London) **408**, 158 (2000).

[6] C. Phatak, A. K. Petford-Long, and M. De Graef, Curr. Opin. Solid State Mater. Sci. **20**, 107 (2016).

[7] W. Coene, G. Janssen, M. Op de Beeck, and D. Van Dyck, Phys. Rev. Lett. **69**, 3743 (1992).

[8] L. J. Allen, W. McBride, N. L. O'Leary, and M. P. Oxley, Ultramicroscopy **100**, 91 (2004).

[9] R. E. Dunin-Borkowski, T. Kasama, and R. J. Harrison, in *Nanocharacterisation*, edited by A. I. Kirkland and S. J. Haigh (Royal Society of Chemistry, London, 2015), Chap. 5, pp. 158–210.

[10] F. Pfeiffer, T. Weitkamp, O. Bunk, and C. David, Nat. Phys. **2**, 258 (2006).

[11] M. McCartney, P. Kruit, A. Buist, and M. Scheinfein, Ultramicroscopy **65**, 179 (1996).

[12] S. B. Mehta and C. J. Sheppard, Opt. Lett. **34**, 1924 (2009).

[13] M. D. de Jonge, B. Hornberger, C. Holzner, D. Legnini, D. Paterson, I. McNulty, C. Jacobsen, and S. Vogt, Phys. Rev. Lett. **100**, 163902 (2008).

[14] N. H. Dekkers and H. de Lang, Optik **41**, 452 (1974).

[15] D. Hamilton and C. Sheppard, J. Microsc. **133**, 27 (1984).

[16] K. Müller, F. F. Krause, A. Béché, M. Schowalter, V. Galioit, S. Löffler, J. Verbeeck, J. Zweck, P. Schattschneider, and A. Rosenauer, Nat. Commun. **5**, 5653 (2014).

[17] H. G. Brown, N. Shibata, H. Sasaki, T. C. Petersen, D. M. Paganin, M. J. Morgan, and S. D. Findlay, Ultramicroscopy **182**, 169 (2017).

[18] N. Shibata, S. D. Findlay, T. Matsumoto, Y. Kohno, T. Seki, G. Sánchez-Santolino, and Y. Ikuhara, Acc. Chem. Res. **50**, 1502 (2017).

[19] J. W. Goodman, *Introduction to Fourier Optics*, 3rd ed. (Roberts and Company, Englewood, 2005).

[20] A. Lubk and J. Zweck, Phys. Rev. A **91**, 023805 (2015).
[21] I. Lazić, E. G. Bosch, and S. Lazar, Ultramicroscopy **160**, 265 (2016).
[22] M. C. Cao, Y. Han, Z. Chen, Y. Jiang, K. X. Nguyen, E. Turgut, G. D. Fuchs, and D. A. Muller, Microscopy **67**, i150 (2017).
[23] J. Zweck, F. Schwarzhuber, J. Wild, and V. Galioit, Ultramicroscopy **168**, 53 (2016).
[24] T. J. Pennycook, A. R. Lupini, H. Yang, M. F. Murfitt, L. Jones, and P. D. Nellist, Ultramicroscopy **151**, 160 (2015).
[25] M. Born and E. Wolf, *Principles of Optics*, 7th (expanded) ed. (Cambridge University Press, Cambridge, 1999).
[26] T. S. McKechnie, *General Theory of Light Propagation and Imaging through the Atmosphere* (Springer International Publishing, Basel, 2016).
[27] J. Chapman, P. Batson, E. Waddell, and R. Ferrier, Ultramicroscopy **3**, 203 (1978).
[28] D. B. Williams and C. B. Carter, *Transmission Electron Microscopy* (Springer, New York, 1996).
[29] N. Shibata, S. Findlay, H. Sasaki, T. Matsumoto, H. Sawada, Y. Kohno, S. Otomo, R. Minato, and Y. Ikuhara, Sci. Rep. **5**, 10040 (2015).
[30] M. De Graef, *Introduction to Conventional Transmission Electron Microscopy* (Cambridge University Press, Cambridge, 2003).
[31] M. Krajnak, *Advanced Detection in Lorentz Microscopy: Pixelated Detection in Differential Phase Contrast Scanning Transmission Electron Microscopy*, Ph.D thesis, University of Glasgow, 2017.
[32] J. N. Chapman, I. R. McFadyen, and S. McVitie, IEEE Trans. Magn. **26**, 1506 (1990).
[33] J. N. Chapman, J. Phys. D **17**, 623 (1984).
[34] T. Uhlig and J. Zweck, Phys. Rev. Lett. **93**, 047203 (2004).
[35] T. Uhlig, M. Rahm, C. Dietrich, R. Höllinger, M. Heumann, D. Weiss, and J. Zweck, Phys. Rev. Lett. **95**, 237205 (2005).
[36] M. J. Donahue and D. G. Porter, *OOMMF User's Guide, Version 1.0*, NISTIR 6376 (National Institute of Standards and Technology, Gaithersburg, 1999).
[37] M. De Graef, N. Nuhfer, and M. McCartney, J. Microsc. **194**, 84 (1999).
[38] S. Majert and H. Kohl, Ultramicroscopy **148**, 81 (2015).
[39] F. Schwarzhuber, P. Melzl, and J. Zweck, Ultramicroscopy **177**, 97 (2017).
[40] See Supplemental Material at http://link.aps.org/supplemental/10.1103/PhysRevA.97.043843 for (a) video showing simulated diffraction patterns over a sequence of probe positions (when $\alpha = 90\ \mu$rad) and (b) video showing simulated diffraction patterns over a sequence of probe positions (when $\alpha = 133\ \mu$rad).
[41] K. Bliokh, I. Ivanov, G. Guzzinati, L. Clark, R. Van Boxem, A. Béché, R. Juchtmans, M. Alonso, P. Schattschneider, F. Nori, and J. Verbeeck, Phys. Rep. **690**, 1 (2017).
[42] J. Verbeeck, H. Tian, and P. Schattschneider, Nature (London) **467**, 301 (2010).
[43] B. J. McMorran, A. Agrawal, I. M. Anderson, A. A. Herzing, H. J. Lezec, J. J. McClelland, and J. Unguris, Science **331**, 192 (2011).
[44] S. Lloyd, M. Babiker, G. Thirunavukkarasu, and J. Yuan, Rev. Mod. Phys. **89**, 035004 (2017).
[45] B. J. McMorran, A. Agrawal, P. A. Ercius, V. Grillo, A. A. Herzing, T. R. Harvey, M. Linck, and J. S. Pierce, Philos. Trans. Royal Soc. A **375**, 20150434 (2017).
[46] L. Clark, A. Béché, G. Guzzinati, A. Lubk, M. Mazilu, R. Van Boxem, and J. Verbeeck, Phys. Rev. Lett. **111**, 064801 (2013).
[47] T. C. Petersen, M. Weyland, D. M. Paganin, T. P. Simula, S. A. Eastwood, and M. J. Morgan, Phys. Rev. Lett. **110**, 033901 (2013).
[48] R. Shiloh, Y. Lereah, Y. Lilach, and A. Arie, Ultramicroscopy **144**, 26 (2014).
[49] A. Béché, R. Winkler, H. Plank, F. Hofer, and J. Verbeeck, Micron **80**, 34 (2016).
[50] A. Béché, R. Van Boxem, G. Van Tendeloo, and J. Verbeeck, Nat. Phys. **10**, 26 (2014).
[51] A. Blackburn and J. Loudon, Ultramicroscopy **136**, 127 (2014).
[52] B. J. McMorran, in *FEMMS 2017 Conference Proceedings* (Frontiers of Electron Microscopy in Materials Science, Johannesburg, 2017), p. 25.
[53] P. Jacquinot and B. Roizen-Dossier, Prog. Opt. **3**, 29 (1964).
[54] K. Müller-Caspary, F. F. Krause, T. Grieb, S. Löffler, M. Schowalter, A. Béché, V. Galioit, D. Marquardt, J. Zweck, P. Schattschneider *et al.*, Ultramicroscopy **178**, 62 (2017).